JOURNAL OF GEOPHYSICAL RESEARCH, VOL. 101, NO. B8, PAGES 18,023–18,041, AUGUST 10, 1996

Recent dueling propagation history at the fastest spreading center, the East Pacific Rise, 26°-32°S

Jun Korenaga

MIT/WHOI Joint Program, Massachusetts Institute of Technology, Cambridge

Richard N. Hey

Hawaii Institute of Geophysics and Planetology, School of Ocean and Earth Science and Technology
University of Hawaii at Manoa, Honolulu

Abstract

The East Pacific Rise (EPR) 26°-32°S, located between the Easter microplate and the Juan Fernandez microplate, has the world's fastest spreading rate and tectonics characterized by dueling ridge propagation. A GLORI-B and Sea Beam 2000 side scan/bathymetry survey, together with other geophysical data collection, was conducted aboard the R/V *Melville* covering an approximately 5° by 5° area centered on this part of EPR. The side scan and bathymetric data reveal the complete geometry of the propagator system. The western and eastern ridges both curve inwardly and are overlapped ~120 km with an offset to overlap ratio of nearly one. Several abandoned ridges and rifts are clearly mapped on the east flank, and a few failed rifts are also mapped near the western ridge tip. A fracture zone discovered south of Easter Island indicates a stage of stable ridge-transform intersection in the past. An inversion with magnetic anomaly vectors was carried out for the area. A resultant magnetic boundary strike map was interpreted with the downward component profiles to construct a magnetic isochron map. The spreading and propagation rates were estimated from the magnetic isochrons. The net southward propagation rate of the western ridge is ~120 km/m.y. for the last 1.9 m.y. The spreading rate of the eastern ridge has been ~150 km/m.y., and its current propagation rate is estimated as ~500 km/m.y. toward the north. Intense asymmetric spreading as high as 30% is observed at both ridges. Together with the side scan and bathymetric data, the magnetic lineations provide significant constraints on the evolution of the propagator system, and a propagation model with cyclic rift failure was applied to model the tectonic evolution during the last 2 m.y. A normal ridge-transform intersection evolved into a nontransform overlapping offset ~1.95 Ma, and the eastern and the western ridges have propagated alternately. The dueling propagation history is characterized by the dominant southward propagation of the western ridge and the transitory propagation events of the eastern ridge with a variety of overlap lengths, widths, and ridge curvatures in the transition zone.

Introduction

The Pacific-Nazca divergent plate boundary, which forms the East Pacific Rise (EPR) 2°40′N-35°S, is the world's fastest seafloor spreading center [*DeMets et al.*, 1994], and it has a distinct contrast of spreading geometry between the northern and southern parts (Figure 1). The northern part is dominated with widely spaced large transform faults and overlapping spreading centers, which is a typical style seen at fast spreading centers, e.g., the Pacific-Cocos [*Macdonald et al.*, 1988*b*] and the Pacific-Antarctic [*Lonsdale*, 1994] plate boundaries. However, the southern section exhibits the most complex spreading pattern ever found, which comprises the Easter microplate [*Handschumacher et al.*, 1981; *Engeln and Stein*, 1984; *Hey et al.*, 1985; *Francheteau et al.*, 1988; *Searle et al.*, 1989; *Zukin and Francheteau*, 1990; *Naar and Hey*, 1991; *Rusby and Searle*, 1995], a large nontransform offset [*Klaus et al.*, 1991], and the Juan Fernandez microplate [*Anderson-Fontana et al.*, 1986; *Francheteau et al.*, 1987; *Yelles-Chaouche et al.*, 1987; *Larson et al.*, 1992].

It has been suggested that the segment of the EPR between these two microplates is offset by one or two transform faults based on the seismicity pattern [*Herron*, 1972; *Engeln and Stein*, 1984; *Hey et al.*, 1985]. A brief SeaMARC II survey, however, revealed the existence of a large, nontransform, overlapping spreading system instead, with the eastern ridge axis propagating rapidly northward and the dominant southward propagation of the western ridge axis [*Klaus et al.*, 1991]. *Klaus et al.* [1991] proposed that this offset was

Paper number 96JB00176.
0148-0227/96/96JB-00176$09.00

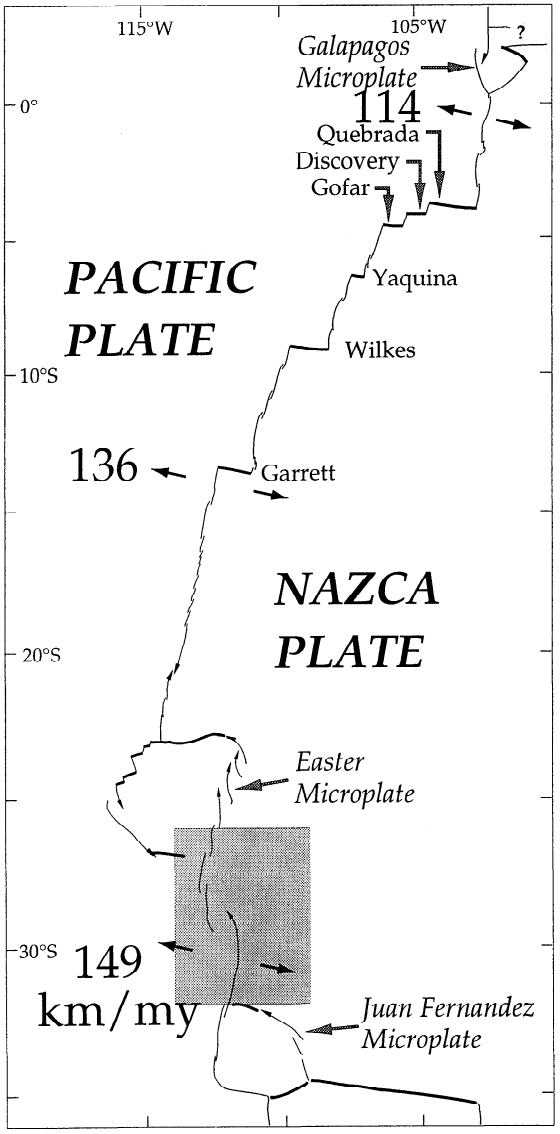

Figure 1. Location map of Leg 5 of the GLORIA expedition. Tectonic boundaries are based on work by *Naar and Hey* [1991] and *Larson et al.* [1992]. Spreading rates are modified from *Naar and Hey* [1989*a*] using revised age of 0.78 Ma for Brunhes/Matuyama reversal [*Shackleton et al.*, 1990; *Hilgen*, 1991*a*; *Baksi et al.*, 1992].

either the largest offset oceanic propagating rift system or the early state of microplate formation. However, most of its complex tectonic history remained unknown due to the limited data coverage.

From February to March 1993, Leg 5 of GLORIA expedition aboard the R/V *Melville* was conducted to investigate the complete dynamics of this EPR offset. Various kinds of geomorphological and geophysical data were collected including GLORI-B [*Somers and Huggett*, 1993] and Sea Beam 2000 side scan/bathymetry, gravity field, and total intensity and vector geomagnetic fields [*Hey et al.*, 1995]. The purpose of this study is to determine the kinematic history of this large nontransform offset, using the magnetic, bathymetric, and side scan data.

Data Acquisition and Processing

The surveyed area extends from the EPR 26°S (the southern area of the Easter microplate) to 32°S (south of the northern boundary of the Juan Fernandez microplate), and from 108°W to 114°30′W in order to cover at least the anomaly 2 chron in age on both sides of the ridge axes. The ship track was designed to optimize the swath coverage of the GLORI-B side scan sonar system in this area, and its spacing is around 28 km (Figure 2).

Bathymetry and Side Scan Data

The initial gridding and data processing of side scan data was done at the Institute of Oceanographic Sciences, Deacon Laboratory. Additional processing at School of Ocean and Earth Science and Technology (SOEST), the University of Hawaii using the Generic Mapping Tools (GMT) program [*Wessel and Smith*, 1991] included geographical coordination with the bathymetry data, histogram equalizing, and stretching the dynamic range of the side scan data to bring out more detail (Figure 3). Strong acoustic backscatter returns (usually associated with recent volcanism or rough surfaces) are white, while weak backscatter areas (usually associated with sedimented areas or shadow zones) are dark. Additional processing details are given by *Johnson* [1996].

This was the first GLORI-B cruise, in which GLORIA swath bathymetry was collected in 24-km-wide swaths. High-resolution Sea Beam bathymetry was also collected, with a narrower swath width (3.46 × water depth). A new processing technique (see details from *Johnson* [1996]) used the Sea Beam 2000 data, centerline bathymetry from other cruises passing through the survey area, and digitized hand-contoured data from previous SeaMARC II and Sea Beam surveys to remove GLORI-B artifacts and produce the color-shaded relief map (Plate 1).

A seafloor fabric chart was constructed from the GLORI-B side scan mosaic and the shaded relief map of the bathymetry (Figure 4).

Magnetic Data

The geomagnetic vector field was obtained with the shipboard three component magnetometer (STCM) [*Isezaki*, 1986]. The STCM system installed on the R/V *Melville* was composed of a triaxial flux gate magnetometer, a horizontal gyroscope, and a Sea Beam 2000 Hippy vertical reference system. The measurement errors of these instruments were 10 nT, 0.1°, and 0.05°, respectively. In order to calibrate the influence of ship body magnetization, three figure eights [e.g., *Korenaga*, 1995] were conducted in the surveyed area (Figure 2). The 12 unknown parameters of ship body magnetization were estimated with least squares inversion for each figure eight (Table 1). Since there was no significant difference in the results of the three trials, these data sets were merged to produce more stable estimation, which was used for the final calibration. The geomagnetic vector anomaly field was then calculated by removing the geomagnetic reference field [*International Association of Geomagnetism and Aeronomy Division V*, 1991]. Owing to the estimation error

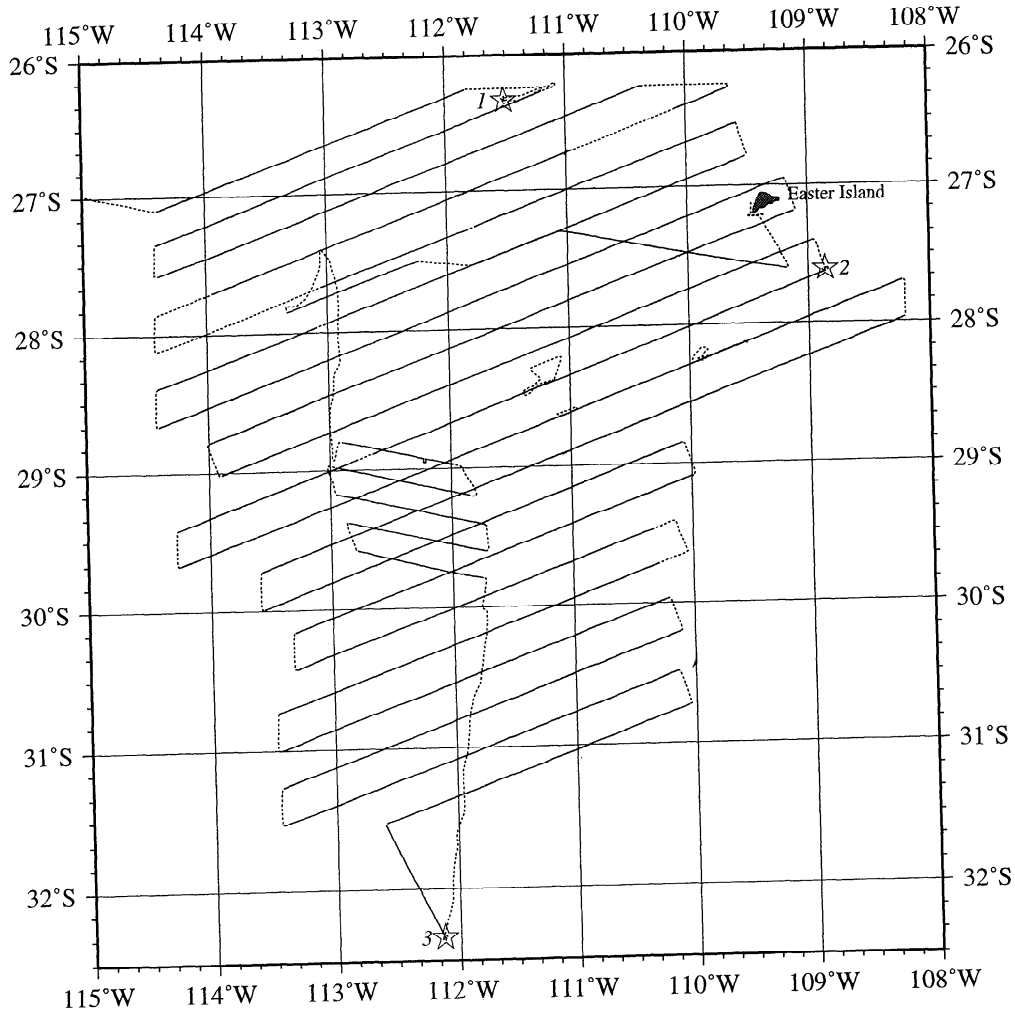

Figure 2. Shiptracks of Leg 5 of the GLORIA expedition are shown as dashed line. Track spacing is 28 km to optimize the swath coverage of the GLORI-B system. The side scan and bathymetry data were collected almost continuously on the ship tracks. Geomagnetic vector field data were obtained on the solid lines. Star marks show locations of figure eights for the shipboard three-component magnetometer operation.

in the ship's magnetization factors, the resultant anomalies suffered from strong bias and drift. These errors were alleviated with further detrending procedure, using straight-line fitting.

According to the noise power spectral analysis [*Korenaga*, 1995], the data quality was estimated, and the vector anomaly data were filtered with the cosine-tapered low-pass filter (maximum amplitude is 0.97, cut wavelength is 4 km, and pass wavelength is 50 km) which was determined by the noise analysis. The absolute error (ΔE_a) and the relative variation error (ΔE_r) of the filtered data are 48 nT and 26 nT/km, respectively.

The filtered geomagnetic vector anomalies, which are shown in Figure 5, were then analyzed with the methods described by *Korenaga* [1995]. The maxima in the profile of intensity of spatial derivative vectors (ISDV) larger than ΔE_r were chosen for the location of magnetic boundaries. The boundary strikes were calculated, and the magnetization contrasts at the boundaries were estimated with the strike information. The three-dimensional (3-D) index was then calculated to test the 2-D assumption in the inversions. Finally, the results of the above processes were merged into a magnetic boundary strike map (MBSM; Figure 6). With a spreading rate of ~150 km/m.y. and an average depth of 3 km, the ISDV cannot resolve magnetic isochrons shorter than the Jaramillo interval (~0.08 m.y.) [*Korenaga*, 1995]. The downward component of the anomalies was upward continued to attenuate the influence of topographic relief, and it was used to supplement the boundary strike map for the interpretation of magnetic lineations (Figure 5d).

Observations and Results

The geomorphologic and magnetic signatures clearly show the entire picture of the overlapping spreading system. The eastern and western ridges are considerably different in their geometry, topography, degree of segmentation, and magnetic character. The overlapped zone has very rough bathymetry and indicates the complicated interaction of these two ridges. Other prominent features such as abandoned ridges, massive

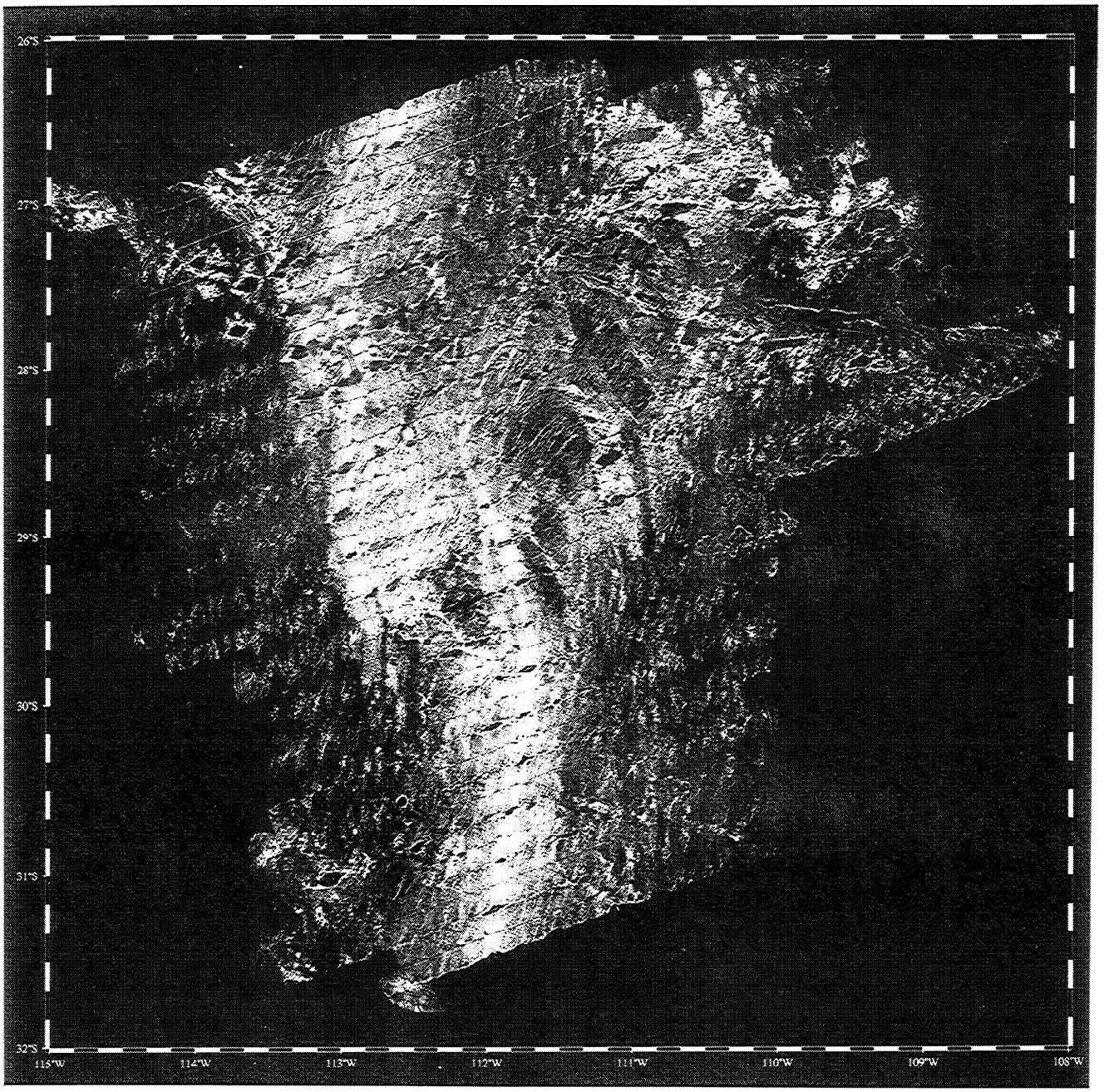

Figure 3. GLORI-B side scan sonar mosaic. Lighter image signifies stronger acoustic backscatter returns. Data have been digitally processed to correct for geometric distortions and to equalize the gain at different ranges. Modified from *Hey et al.* [1995] and *Johnson* [1996].

seamount swarms, and a fracture zone were also mapped. In the following sections, the seafloor fabric, topography, and magnetic character of these elements are described in detail, and the Vine-Mathews type magnetic lineations are identified based on the magnetization map and the downward component profiles of geomagnetic vector anomalies. Finally, a possible kinematic model is constructed for the evolution of this overlapping spreading system.

Western Ridge

The western ridge has broad V-shaped shallow bathymetry (Plate 1). The ridge flanks above 2800 m contours are 300 km wide at 27°S, and the width gradually reduces southward, e.g., 98 km wide at 28°S and 7 km wide at 29°30′S. The eastern end of this shallow zone around 27°S seems to be inflated by off-axis volcanism.

Four major segments are recognized along the ridge axis, and the right-stepping and left-stepping offsets alternatively bound these segments. The segments are tentatively numbered as W1 to W4 southward (Figure 4). The W1 and W2 segments form the southern part of the eastern boundary of the Easter microplate. They overlap at ~26°40′S, and the overlap length and the offset width of the discontinuity are 20 km and 24 km, respectively. The geometry of the dis-

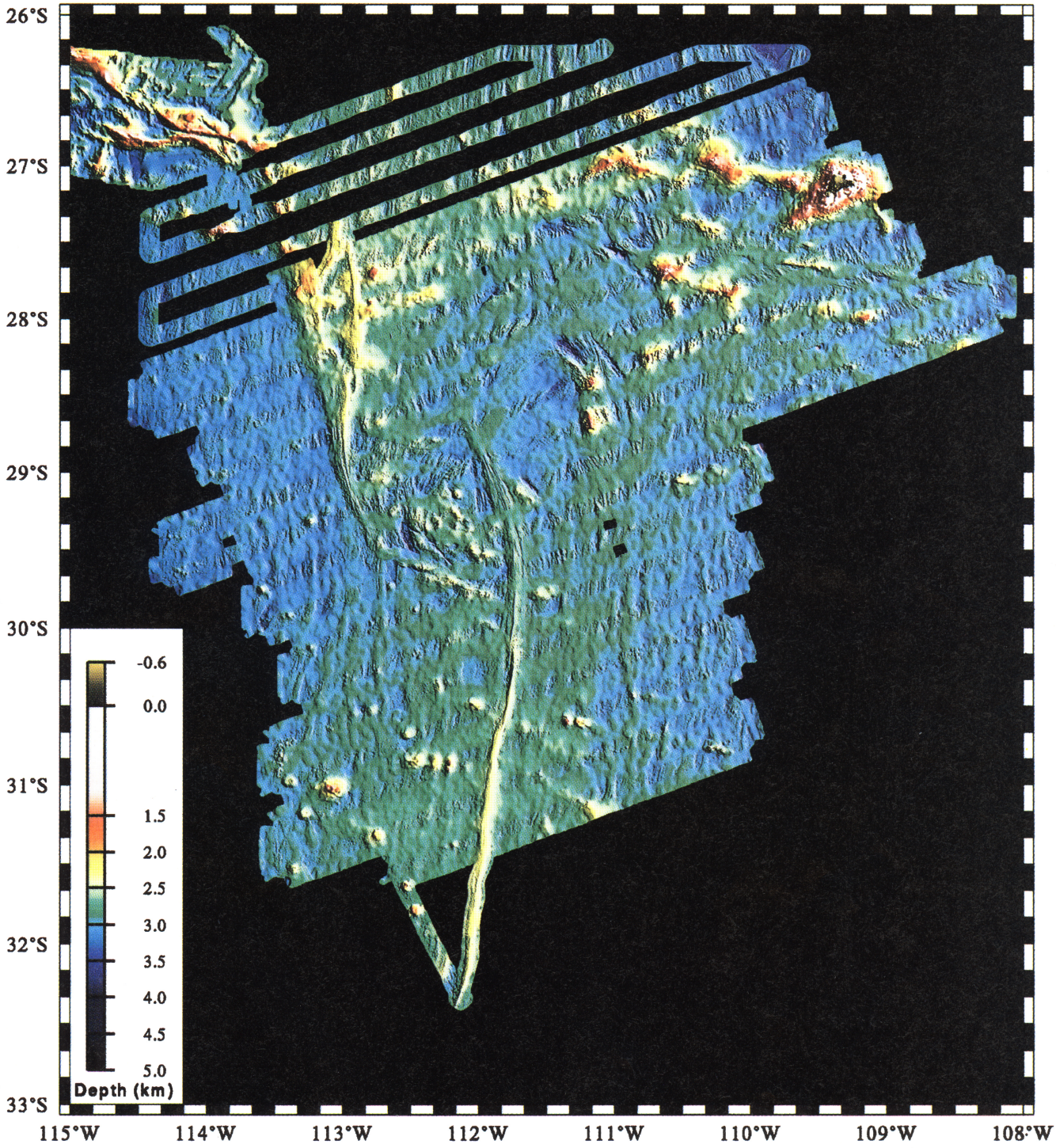

Plate 1. Color shaded-relief bathymetry map illuminated from northeast. High-resolution Sea Beam 2000 bathymetric swaths are overlaid onto wider GLORI-B swaths. Southwest margin of Easter microplate were digitized from hand-contoured SeaMARC II data [*Naar and Hey*, 1991]. Modified from *Hey et al.* [1995] and *Johnson* [1996].

continuity is significantly deviated from a large overlapping spreading center (OSC) and may be classified as a propagating rift system [*Macdonald et al.*, 1988*b*]. The W2 segment has an S-curved axis; its trend changes from N33°E at the northern end to N10°E at the middle and to N30°E at the southern end. In contrast, the W3 segment has a nearly uniform N-S trend. The W2 and W3 segments overlap at ~27°40′S with an overlap length of 28 km and an offset of ~13 km. This discontinuity can be considered as a large OSC although the W2 segment curves outward. An inward hook-shaped curvature is expected at a simple OSC according to previous observations elsewhere [e.g., *Macdonald et al.*,

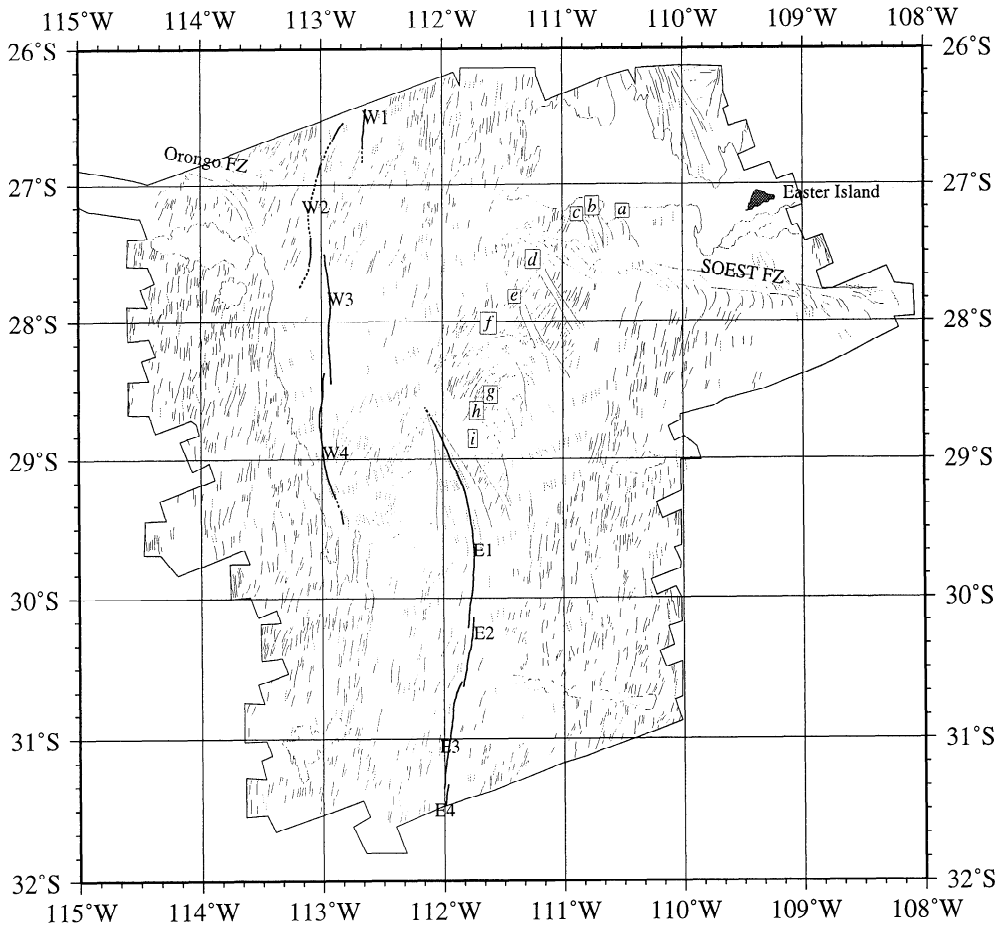

Figure 4. Seafloor fabric chart. Several important tectonic components, such as ridge axis discontinuities, pseudofaults, fracture zone, and abandoned ridges, are recognized with side scan and bathymetry data. Thick lines show ridge segments identified with bathymetry, and the segments are labeled as W1-W4 for the western ridge and E1-E4 for the eastern ridge. Dashed lines indicate presumed location of ridge axis, which are not clear in both side scan and bathymetry data. Thin lines show seafloor fabric recognized in the side scan data, and thin dashed lines are based on shaded relief bathymetry. Abandoned ridges and rifts are observed on the east flank and are labeled from a to i. Blank area enclosed with thin lines shows seafloor covered with seamounts and/or lava flows.

1984] and to fracture mechanics [*Pollard and Aydin*, 1984; *Sempere and Macdonald*, 1986], and the unusual curvature may be attributed to the stress field created by the microplate rotation [*Schouten et al.*, 1993]. The southern end of the W3 segment overlaps with the W4 segment at 28°27′S. The overlap length and the offset width are 10 km and 7 km, respectively. The W4 segment begins to bend eastward at ~28°50′S, which corresponds to the overlap with the eastern ridge, and it seems to end at ~29°30′S. Several short rifts are observed to the southeast of the W4 segment end.

From the middle of the W2 segment to the W4 segment, the axial depth is relatively higher than the other parts (>2200 m). As clearly shown in the bathymetric map of *Naar and Hey* [1991], this regional topographic high seems to be connected to that of the southwest rift of the Easter microplate. Compressive stress near the southwest rift, which is sug-

Table 1. Ship Magnetization Factors

	a_{xx}	a_{xy}	a_{xz}	a_{yx}	a_{yy}	a_{yz}	a_{zx}	a_{zy}	a_{zz}	h_{px}	h_{py}	h_{pz}
1	-0.1026	-0.0763	0.0399	0.1380	-0.0686	0.0067	-0.0433	-0.2171	0.1155	-9753	-8939	26886
2	-0.0980	-0.0760	-0.0127	0.1406	-0.0641	0.0326	-0.0450	-0.2168	0.1582	-10750	-8360	27591
3	-0.1082	-0.0882	-0.0071	0.1512	-0.0752	0.0704	-0.0508	-0.2120	0.3639	-10174	-7022	32576
Final	-0.1045	-0.0739	-0.0997	0.1412	-0.0713	-0.0387	-0.0467	-0.2189	0.1938	-12536	-9776	28418

The a_{ij} and h_{pi} $(i, j = x, y, z)$ are the elements of the induced magnetization matrix A and the permanent magnetization vector H_p, respectively. Figure eight locations 1–3 are shown in Figure 2, and 12 parameters are estimated for each figure eight. Final calibration uses all data sets of three figure eights for more stable estimation.

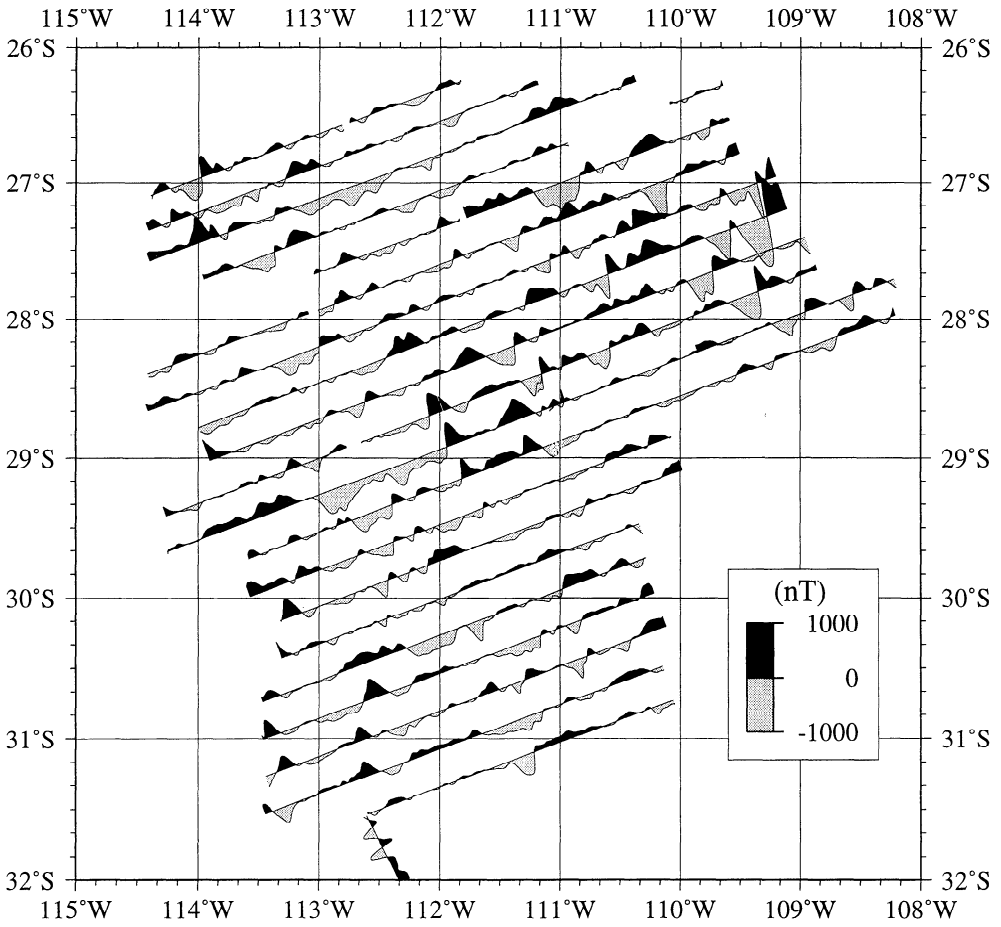

Figure 5a. Wiggle map of filtered geomagnetic vector anomalies for northward component. Positive anomalies are shown in black, and negative anomalies are lightly shaded. Wiggle scale is shown in the inset, and its unit is nanoteslas. The data on the short tracks in the overlapped zone are not shown here.

gested by the location of the Pacific-Easter Euler pole [*Naar and Hey*, 1991], may explain the elevated topography around the southwest rift, but it does not account for the anomalous ridge axis height of the western ridge. The seamount chain observed west of the ridge ~27°20′S implies intensive volcanic activity, which may have influenced the volcanism along the ridge axis. The axis of the W4 segment exhibits southward gradual deepening from 2100 m to 2600 m, and the rifts located southeast to the segment are as deep as 3500 m.

The Brunhes to 2A magnetic isochrons are identified along the western ridge axis (Figure 7). The Brunhes chron (0.00-0.78 Ma [*Shackleton et al.*, 1990; *Hilgen*, 1991*a*, 1991*b*; *Baksi et al.*, 1992]) widens southward and is the widest around 28°10′S. Then it rapidly narrows toward the ridge tip. A discontinuity in the Brunhes-Matuyama (B/M) boundary on the east flank around 28°S may be a trace of northward propagation of the W3 segment. The Jaramillo chron (0.99-1.07 Ma) on the west flank curves toward the ridge axis, while the east one seems to bend slightly away from the axis (~27°20′S). The inner and outer pseudofaults of the western ridge are estimated from the shape of the Brunhes chron, and the angle between the pseudofaults is ~52°. The anomaly 2 chron (1.79-1.95 Ma) is identified on the east flank, though it cannot be traced south of 27°10′S. The anomaly 2A chron (2.60-3.04 Ma) is also identified on the east flank, and its west boundary ends up at 27°30′S. Its eastern boundary is disrupted by off-axis volcanism associated with Easter Island. The short normal polarity chron between 2 and 2A (anomaly 2R-1; 2.14-2.15 Ma) cannot be identified because of insufficient data.

The position of the ridge axis in the Brunhes chron indicates intense asymmetric spreading to the east, especially along the W2 to the W4 segments. The ridge flank topography also shows prominent asymmetry; the east flank has a much broader shallow area than the west one, and its slope variation is less irregular.

Most of the magnetization contrasts at the polarity reversal boundaries are around 10 A/m, with a small variation of ±3 A/m (Figure 6). The magnetic boundary west of the W4 segment has an exceptionally high contrast of 20 A/m, which is the boundary of the positively magnetized seafloor (Brunhes) created by the western ridge and the negatively magnetized and older seafloor (between Jaramillo and anomaly 2) created by the eastern ridge (Figure 7). High 3-D indices are observed in several locations (Figure 6), and they seem to correlate well with the ridge axis discontinuities and large-scale off-axis volcanism (Plate 1).

Eastern Ridge

In contrast to the intensively fragmented western ridge, the eastern ridge exhibits more continuous structure (Figure 4). The ridge axis is disrupted with small OSCs at 30°10′S,

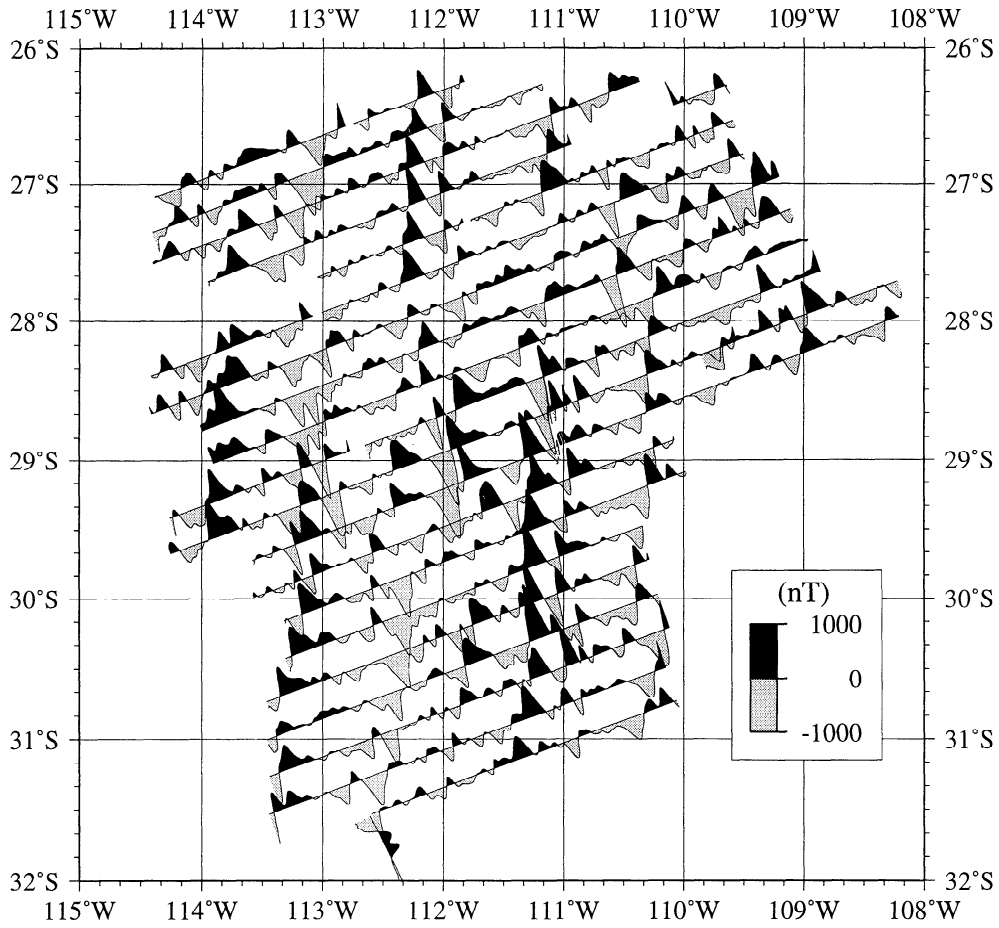

Figure 5b. Eastward component.

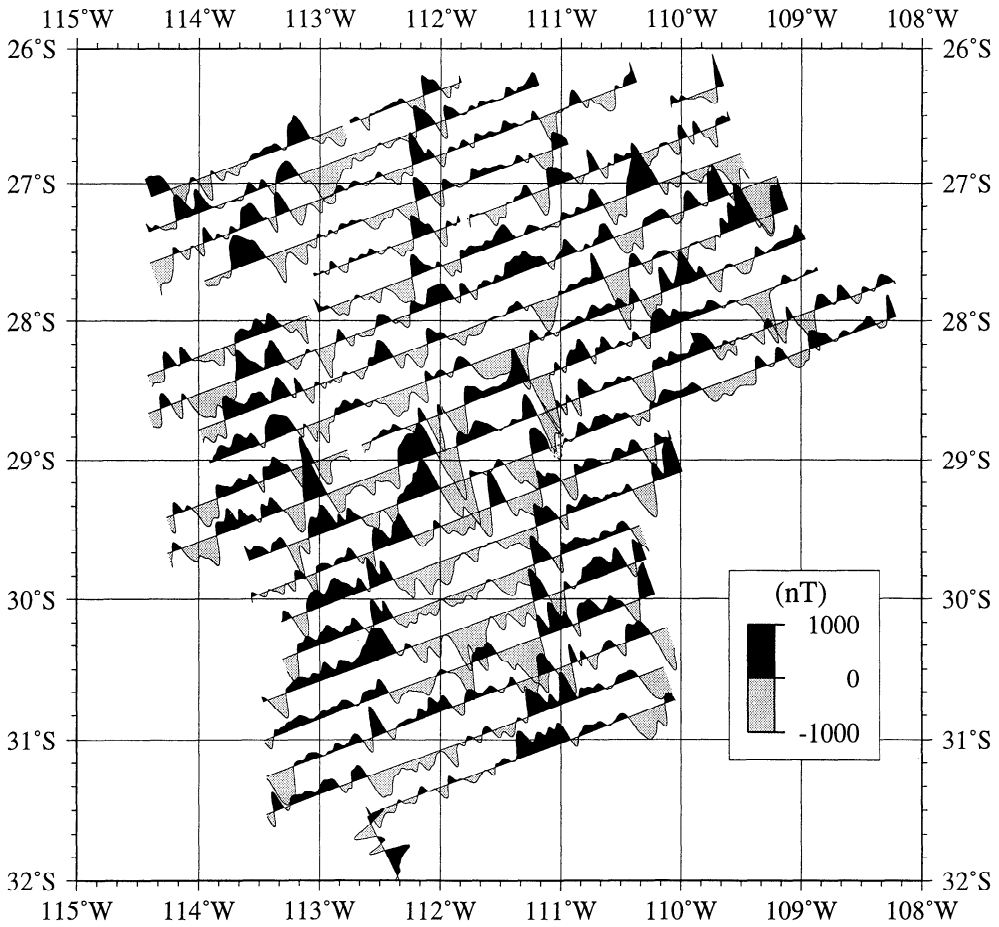

Figure 5c. Downward component.

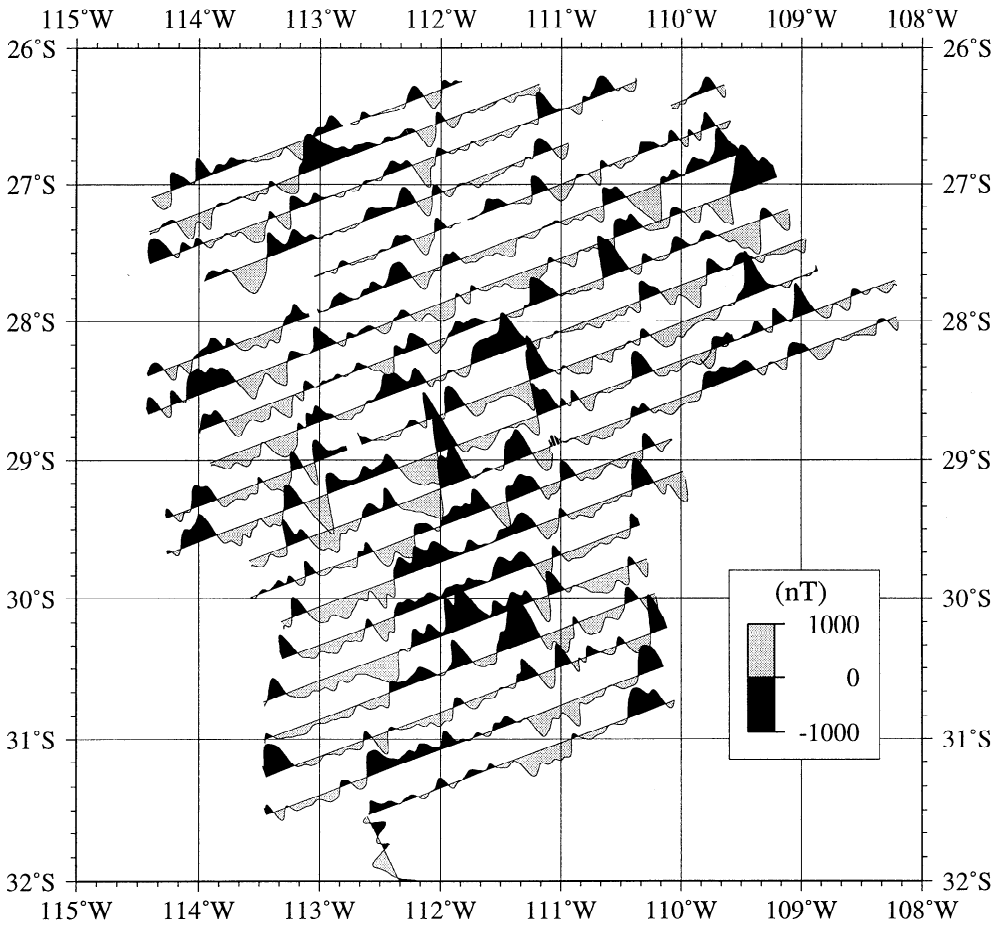

Figure 5d. Downward component which was upward continued with Sea Beam 2000 center beam bathymetry to attenuate the influence of topographic relief. The sign of anomaly is reversed here for magnetic anomaly interpretation.

30°40′S, and 31°20′S. The sense of the stepping at the discontinuities alternates between right and left. Around the northern ridge tip, the axis trend is N30°W then gradually changes to N20°W. Then the axis crooks to N03°E, corresponding to the end of the overlapped zone with the western ridge. The southern part of the ridge axis, with a general trend of N07°E, merges into the western boundary of the Juan Fernandez microplate at 31°31′S [*Larson et al.*, 1992].

The northern and southern parts of the ridge have different bathymetric features both in along-axis and across-axis directions (Plate 1). The axial depth profile of the northern part shows southward decrease from 2700 m at the tip to 2600 m at the middle and 2300 m at the southern edge [see also *Klaus et al.*, 1991, Figure 7]. On the other hand, the southern part keeps a nearly constant axial depth of 2350 m. The ridge flanks along the southern part are shallower than those along the northern segment. In addition, the southern ridge flanks seem to be more symmetrical than the northern ones. The asymmetric topography on the northern flanks may be related to the complex history of the overlapped zone as described later. Although the northern ridge has such an along-axis gradient, no graben structure is observed at its tip. It is puzzling because a graben structure resulting from the viscous head loss of ascending magma is expected at a propagating rift tip [*Phipps Morgan and Parmentier*, 1985]. Some lava flows from the nearby seamounts [*Klaus et al.*, 1991] may have filled up a rift tip graben.

On both ridge flanks, the Brunhes to 2A magnetic chrons are identified, though some of them fail to show their complete shapes due to the limitation of the surveyed area (Figure 7). The eastern ridge Brunhes chron has a two-pronged shape, and the west prong along the ridge axis, which extends northwest of the east prong, indicates recent northward propagation. The wedged boundary of the west prong defines the inner and outer pseudofaults, which intersect at 17°. The east prong implies an abandoned ridge, which is discussed later. The Jaramillo chron on the east flank curves as the eastern ridge axis does and disappears around 28°15′S. The west Jaramillo chron is identified up to ~29°30′S where it is disrupted by the Brunhes chron of the western ridge. On the east flank, the anomaly 2 chron crosses over the newly mapped fracture zone and extends to 27°S, while the anomaly 2R-1 and 2A chrons stay south of the fracture zone. The southern ends of the anomaly 2 and 2R-1 chrons on the west flank are limited by the outer pseudofault of the western ridge. A normal chron observed from 27°50′S, 111°10′W to 28°40′S, 111°50′S is identified as the anomaly 2 chron, which was originally formed on the west flank and then was transferred to the east flank by the southward propagation of the western ridge. The 2A chron to the west is partly iden-

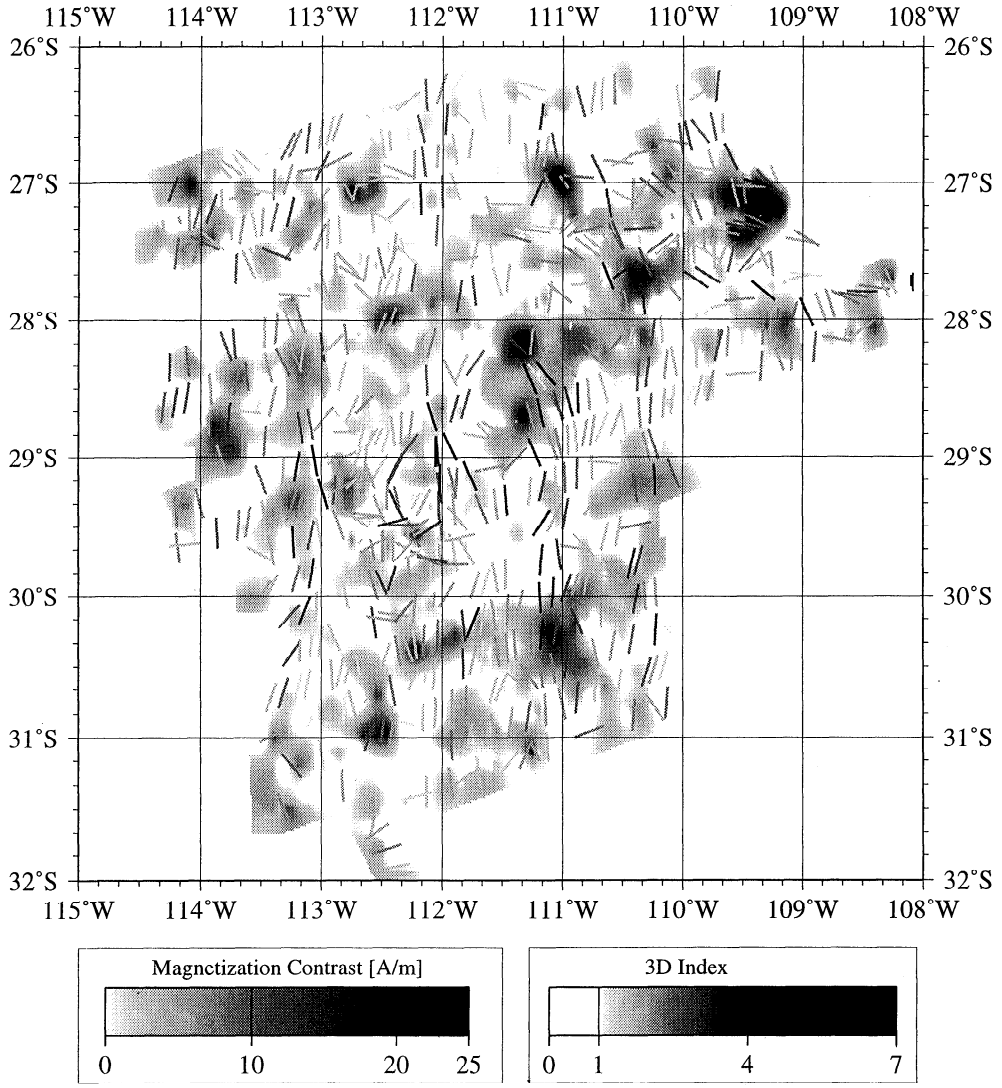

Figure 6. Magnetic boundary strike map (MBSM). Three-dimensional index profiles were gridded to make gray scale image of three-dimensionality. Darker shade signifies higher deviation from two-dimensionality. Magnetic boundary information was superposed on this image. Direction of bar shows the declination of boundary strike, and its length varies with the cosine of the inclination. Bar shades indicate intensity of magnetization contrasts at boundaries; darker bar signifies magnetic boundary with strong contrast. Strikes with angular standard deviation less than 10° are shown.

tified between 27°30′S and 29°30′S. The geometry of these identified isochrons is the key to the tectonic history of this area and plays a crucial role in the later kinematic modeling. Several discontinuities observed in these isochrons indicate ridge axis discontinuities in the past. They may constrain the evolution of the eastern ridge segmentation though the magnetic data here have only low resolution for this purpose.

Strong magnetization contrasts as high as 20 A/m are seen at two locations (Figure 6); one is around the eastern ridge tip, and the other around the tip of the east Jaramillo chron. Although there have been no rock samples dredged from the eastern ridge tip, the high magnetization contrast is probably a result of Fe-Ti basalts, which are common at other propagating rift tips [*Christie and Sinton*, 1981; *Sinton et al.*, 1983]. In general, the boundaries of the polarity chrons have higher magnetization contrasts than those associated with the western ridge; the averaged contrast, excluding the above anomalous high values, is 14 A/m.

Overlapped Zone

The western and eastern ridges overlap from 28°40′S to 29°30′S (Figure 4). Both the length and width of the overlap are ~120 km so that the length to width ratio is ~1:1. The topography of this region is highly complicated with seamounts overlaying the southern portion and multiple rifts in the southwestern portion. The seafloor reflectivity of the seamounts is lower than that of the surrounding seafloor, which indicates off-axis volcanism in the past. The rifts may be the traces of previous propagation events of the western ridge, considering a deep rift is often observed at the tip of a propagating ridge [e.g., *Hey et al.*, 1986; *Naar and Hey*, 1991]. The seafloor fabric in this region shows a general NE-

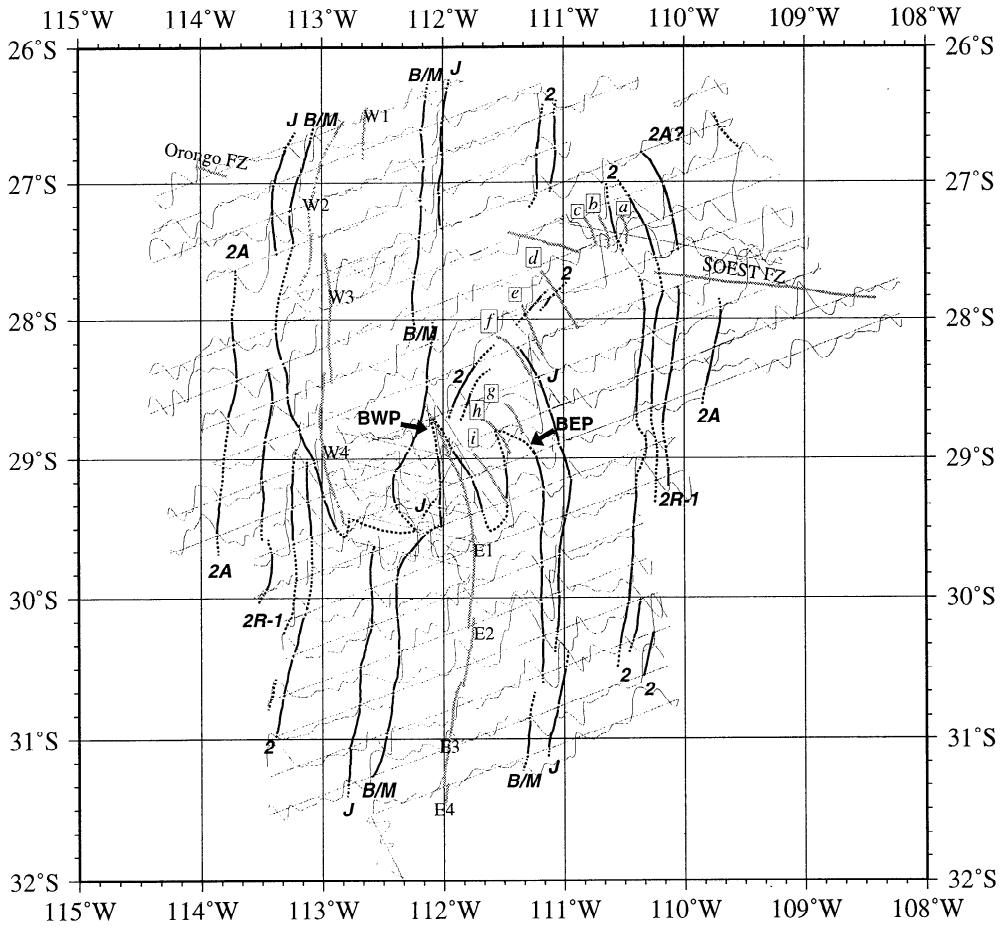

Figure 7. Magnetic isochron map. Isochrons were identified based on both MBSM (Figure 6) and upward continued downward component (Figure 5d) shown as wiggles. BWP and BEP are the western and eastern prongs of the Brunhes chron of the eastern ridge. Crosses show anomaly picks along tracks, and lines refer to MBSM. Dotted lines signify identification of less certainty. Gray lines show basic tectonic features such as ridge segments, abandoned ridges, and fracture zones (Figure 4).

SW trend, though the fabric pattern is frequently disturbed with the trend variation from almost N-S to N60°E.

The Brunhes chron of the western ridge dominates the overlapped zone. Successive westward ridge jumps of the western ridge in this zone are suggested by the intensive asymmetric spreading of the W4 segment and by several rifts observed around the Brunhes chron tip. There is a slight indication of the Jaramillo chron around 29°20′S, 112°10′W, which was probably transferred from the western flank of the eastern ridge.

Abandoned Ridges and Rifts

Several abandoned ridges and rifts (AR; labeled as a–i in Figure 4) are identified on the east flank, based on the topography and the side scan data, and some of them are also seen in the magnetic lineations (Figure 7). The disposition of the ARs resembles the geometry of the failed rifts in the rift propagation model with cyclic rift failure [*Wilson*, 1990], and it is consistent with the dominant southward propagation of the western ridge [*Klaus et al.*, 1991; *Naar and Hey*, 1991]. The ARs, however, do not align exactly, and their tips do not have the same curvature. The deviation from the simple Wilson model indicates several perturbations such as the propagation of the eastern ridge and changes in the offset length and width of the overlap.

ARs a, b, and c are located north of the fracture zone and seem to be created by three successive rift failures with a short cycle. The north end of the anomaly 2 chron on the east flank is identified close to these ARs. The anomaly 2 chron is extended across the fracture zone because the normal anomaly identified here does not fit the anomaly sequence of the western ridge and because the interpretation is consistent with the morphological observation. The low three-dimensionality of the observed anomaly is evidence that this magnetic lineation is reliable, rather than a seamount-related magnetic anomaly.

ARs d and e have the almost same curvature, and their tips are obscure. The curvature of AR f is slightly more acute, and the seafloor fabric near AR f has more eastward orientation. In addition, the anomalously high topographic expression, strong seafloor reflectivity, and strong magnetization contrast characterize AR f. The Jaramillo isochron on the west flank corresponds to AR f, and its evolution is an important stage in the kinematic modeling discussed later.

AR g is located ~50 km south of AR f, suggesting a

long ridge jump. ARs g and h bend similarly while AR i has gentler curvature which implies the lengthening of the overlapping zone between ARs h and i.

Fracture Zone

The discontinuities in the magnetic isochrons enclosing the Easter microplate have implied a fracture zone near Easter Island [see *Naar and Hey*, 1991, Figure 6]. The side scan images clearly exhibit the SOEST fracture zone [*Hey et al.*, 1995] south of Easter Island (Figure 3). Some magnetic boundary strikes on the east flank between 27°S and 28°S have a northwest trend and correspond to the topographic relief of the fracture zone (Figure 6). This newly discovered fracture zone extends from 27°20′S, 111°30′W to at least 108°30′W (the eastern limit of the survey). Its width varies from a few to 10 km, and the depth is around 3300 m except for the shallower portions around 110°30′W near the ARs and seamounts (Plate 1). The trend of the fracture zone is ~N82°W south of Easter Island and changes to ~N73°W to the west of the disrupted portion near the ARs. The trend predicted by the global plate motion model (NUVEL-1) [*DeMets et al.*, 1990, 1994] is ~N79°W (Pacific-Nazca relative motion) at this location. The change in the trend and the discrepancy between the observed and the predicted trends are discussed later.

It is unclear that this fracture zone has its counterpart on the west flank; it may exist south of the Orongo fracture zone, around 27°S, 114°W, where all the available data sets such as bathymetry, magnetic anomalies, and side scan images show very complex structure. This region includes the southern triple junction of the Easter microplate [*Naar and Hey*, 1991], and simple fracture zone structure may not be expected. An additional fracture zone west of Easter Island around 27°S (Figure 3) is thought to be related to the southern boundary of the Easter microplate [*Hey et al.*, 1995] but is not modeled in this paper.

Seamount Distribution

Most of the highly three-dimensional magnetic fields in Figure 6 correlate to the magnetic fields produced by the seamounts (Plate 1). The northern part of the surveyed area is overlaid with more massive seamounts than the southern part, such as the eastern part of the Ahu volcanic field [*Hagen et al.*, 1990] around Easter Island, the seamount chain on the south of the SOEST fracture zone, and the seamounts west of the outer pseudofault of the western ridge (Plate 1). As well as a possible Easter hotspot in the Ahu volcanic field, these seamount chains may have important implications for the evolution of the Easter microplate and the nontransform offset studied herein. The age information of those seamount chains is required to consider their magmatic influence on the tectonic evolution of the spreading segments.

Plate Kinematics

Spreading and propagating rates. To estimate the recent spreading rate at the eastern ridge, the distances between the ridge axis and the anomaly picks are measured, assuming orthogonal spreading (~N97°E). NUVEL-1 predicts the spreading direction of ~N102°E for the eastern ridge so that there may be small obliquity in spreading and the estimated spreading rates provide the minimum bounds. The anomaly picks which fall onto the skewed part such as the northern ridge tip are not used so that most picks are sampled to the south of 29°30′S. The measured distances are somewhat scattered, probably due to errors in isochron identification, and thus the measurements that belong to the same reversal boundary are averaged. Because of intense ridge axis segmentation, the same approach cannot be applied to the western ridge. Instead, the distances between the same reversal boundaries on the flanks are measured in the spreading direction predicted by NUVEL-1 (~N103°E) to estimate the total spreading rate. The southern portion of the western ridge has no Jaramillo chron, indicating this portion has been created by ridge propagation during the Brunhes Epoch. Thus the measurement is conducted only along the northern portion near 27°S. The resultant spreading rates are shown in Table 2. Except for the slight decrease observed around 2.0 Ma, the eastern ridge has kept its spreading rate as high as ~150 km/m.y. since 2.5 Ma, consistent with the prediction of the global plate motion model [*DeMets et al.*, 1994]. The calculated asymmetry in the spreading rates of the eastern ridge has scattered values. Considering the discontinuities recognized in the magnetic lineations, the number of sampled points for spreading rate measurement may not be enough for reliable determination of asymmetric spreading. It is natural that much slower spreading has occurred on the western ridge (Easter-Nazca plate boundary) because there is another ridge system located to the northwest (Pacific-Easter plate

Table 2. Estimated Half and Full Spreading Rates

Location	Section	Period, Ma					
		-0.78	-1.03	-1.79	-1.95	-2.14	-2.60
Eastern Ridge	east flank	76 (6)	73 (6)	74 (5)	68 (2)	—	—
(south of 29°30′S)	west flank	71 (6)	77 (7)	75 (6)	73 (3)	75 (2)	79 (1)
	asymmetry	-3.4	2.7	0.7	3.5	—	—
	total	147 (12)	150 (13)	149 (11)	141 (5)	—	—
Western Ridge (27°S)	total	135 (2)	132 (2)	—	—	—	—

All periods shown begin at the present time. The unit of spreading rates is km/m.y., and the number of sampled distances averaged for estimation is shown in parentheses. Asymmetry is measured as percent difference in half rates divided by total spreading rate. Positive asymmetry corresponds with faster rates to the west. Note that western ridge at 27°S is Easter-Nazca plate boundary, while eastern ridge is Pacific-Nazca plate boundary.

boundary), which constitutes the southwest rift of the Easter microplate [*Naar and Hey*, 1991]. Any spreading in the failing rifts to the west would also produce slower spreading on the western ridge.

The currently propagating eastern ridge axis has an angle of ~17° between the inner and outer pseudofaults. Because a propagation rate p, a spreading half rate s, and a tip angle α have a simple relation expressed as $\alpha = 2\arctan(s/p)$ [e.g., *Hey et al.*, 1986], the propagating rate of the eastern ridge is estimated to be ~500 km/m.y. The western ridge is currently failing as the eastern ridge propagates. The short rifts located to the southeast of the W4 segment (Figure 4) may be abandoned rift tips of the western ridge. However, it is obvious in the magnetic lineations that its southward propagation has dominated over this region. Because the ridge tip is located 230 km away from the fracture zone, the net propagation rate of the western ridge is inferred to be ~120 km/m.y., assuming that the western ridge began its propagation since the anomaly 2 period, i.e., 1.9 Ma.

Kinematic modeling. The recent northward propagation of the eastern ridge is supported by the magnetic lineation, the topography, and the side scan lineaments [*Klaus et al.*, 1991; *Hey et al.*, 1995]. The dominant southward propagation of the western ridge is obvious in the side scan reflectivity (Figure 3) and the shape of the Brunhes chron (Figure 7). The Jaramillo chrons of the western ridge extend south of the SOEST fracture zone, while the anomaly 2 chron is only seen north of the fracture zone. This means that the propagation initiated sometime between anomaly 2 and Jaramillo. The ARs on the east flank seem to be the failed rifts of the eastern ridge resulting from this southward propagation. The anomaly 2 chron and ARs a, b, and c extend north of the fracture zone. This suggests that the eastern ridge first broke a normal ridge-transform-intersection (RTI) by making a nontransform offset before the anomaly 2 period and that the eastern ridge then failed as the western ridge began to propagate succeedingly. The change in trend of the SOEST fracture zone near 110°40′W could indicate a clockwise rotation of Pacific-Nazca motion around 2 Ma or could have resulted from rotation in the overlap zone produced by this initial northward propagation. The other ARs roughly align to the southwest of ARs a, b, and c, which can be explained as the cyclic rift failure of the eastern ridge. However, AR f is prominent for its ambient seafloor fabric orientation and the magnetic contrast at the tip, both of which imply that the eastern ridge may have propagated a short distance to the north during the Jaramillo period. The two-pronged Brunhes chron of the eastern ridge and AR i located in between (Figure 7) signify that the failing rift converted to the currently propagating ridge in the middle of the Brunhes Epoch.

Wilson [1990] proposed a rift propagation model with cyclic rift failure, which explains observations in more detail than the previous models [*Hey et al.*, 1980; *McKenzie*, 1986]. The model was extended for dueling propagation (D. S. Wilson, personal communication, 1993), and it has been applied to OSC's evolution by several authors [e.g., *Carbotte and Macdonald*, 1992; *Perram et al.*, 1993]. To explain all the tectonic features described above, a possible kinematics of this dueling propagator system is reconstructed using this extended rift propagation model. The available data sets are not sufficient to resolve the fine-scale evolution of the ridge axis segmentation, so each ridge axis is simplified as being continuous. Although asymmetric spreading seems to have been persistent throughout the period of interest (Table 2), it

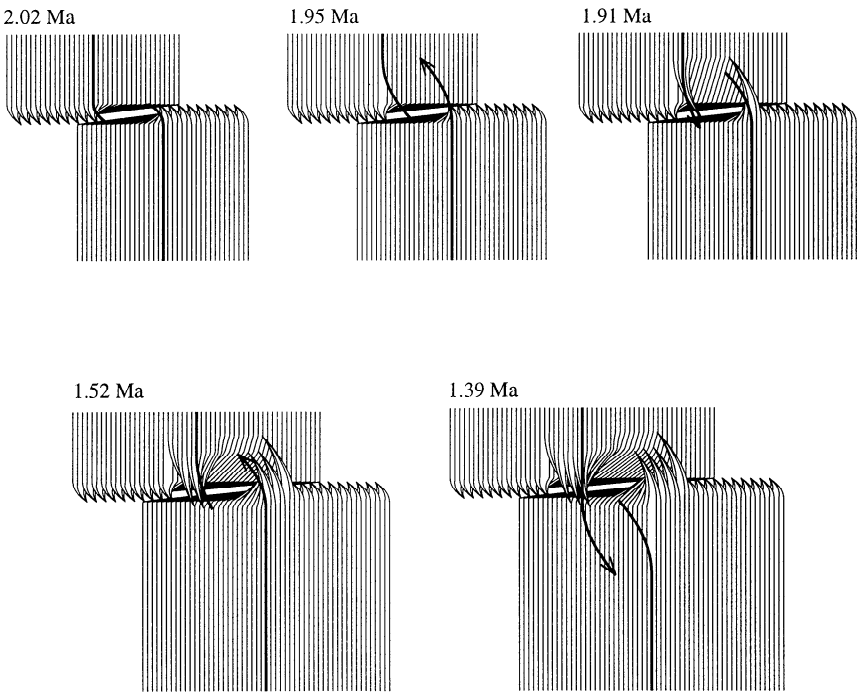

Figure 8a. Kinematic model for evolution of the dueling propagator near 29°S since 2 Ma. At 1.95 Ma, a normal RTI was broken, and dueling propagation was initiated. Heavy line shows position of ridge axis, and light lines show isochrons every ~0.075 m.y. Modeling algorithm was provided by D. S. Wilson.

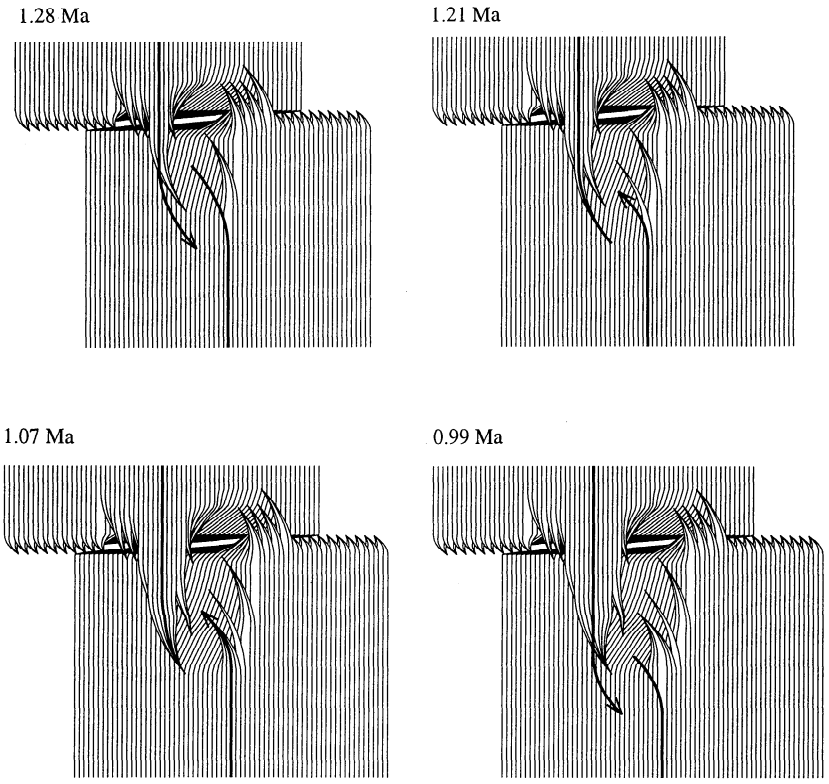

Figure 8b. Until ~1.2 Ma, the western ridge had propagated southward, and then the eastern ridge propagated northward briefly (~0.2 m.y.). The orientation of the seafloor fabric was perturbed by this northward propagation. The western ridge resumed its southward propagation ~1.0 Ma.

is introduced only during the Brunhes epoch for simplicity. Thirty percent asymmetric spreading to the east is used for the western ridge. The same asymmetry with opposite sense is used for the eastern ridge since 0.31 Ma in order to account for the roughly 30% asymmetry of the pseudofaults relative to the present ridge axis. To match the observed total asymmetry during the Brunhes epoch (-3.4 %), 26% asymmetric spreading of east directive is introduced for the period 0.31-0.78 Ma. Several stages in the kinematic model are shown in Figure 8. In this model, the two ridges had formed a normal RTI before ~1.95 Ma. The observed fracture zone shows that this structure had been maintained for at least ~1 m.y. Then the eastern ridge began to propagate to the north, making an overlapped zone with the western ridge (Figure 8a). Successively, the western ridge commenced its southward propagation, and a rift failure repeated at the eastern ridge tip. Around 1.2 Ma, the polarity of propagation changed, and the eastern ridge began to propagate (Figure 8b). It is noted that a stalling period in the southward propagation is sufficient to create the observed change in the seafloor fabric around AR f. The high magnetization contrast at the AR may simply result from the positive magnetization of the tip and the negative magnetization of the surrounding seafloor. However, the east prong of the Brunhes chron of the eastern ridge, which has a similar geometric situation, has a lower magnetization contrast than the contrasts at the west prong and AR f. Thus the northward propagation scenario is preferred to explain both the seafloor fabric and the magnetization contrasts. This northward propagation continued only for ~0.2 m.y., and the western ridge resumed propagating southward. At ~0.3 Ma, the eastern ridge began propagating northward once more until the present (Figure 8c). It is noted that the rift failure, which is modeled here to occur instantaneously, must be a very rapid propagation event in a finite period and that the estimated propagation rate for the eastern ridge (500 km/yr) is in fact of net propagation including the rapid propagation around 0.31 Ma and the succeeding much slower ridge propagation. This kinematic model reproduces the observed seafloor fabric and magnetic lineations to the first-order. Naturally, the modeling conducted here is not unique. After a number of trials with different families of models, however, it became clear that other models with different parameter settings tended to deviate quickly from the evolution shown in Figure 8 and resulted in significantly different geometries at the end of the runs. The model presented here is a representative of the family whose final configuration resembles the observations most closely, and it seems to succeed in outlining the first-order evolution of this dueling propagator system.

Discussion

Difference From Previous Work

Klaus et al. [1991] identified the outer pseudofault of the eastern ridge differently from this study, resulting in a propagating tip angle of ~33°, while this study shows the angle of ~17°. Their identification was based mainly on the short fragment of trough located near 29°00′S, 111°40′W, and it was confronted with the difficulty that seafloor inside their

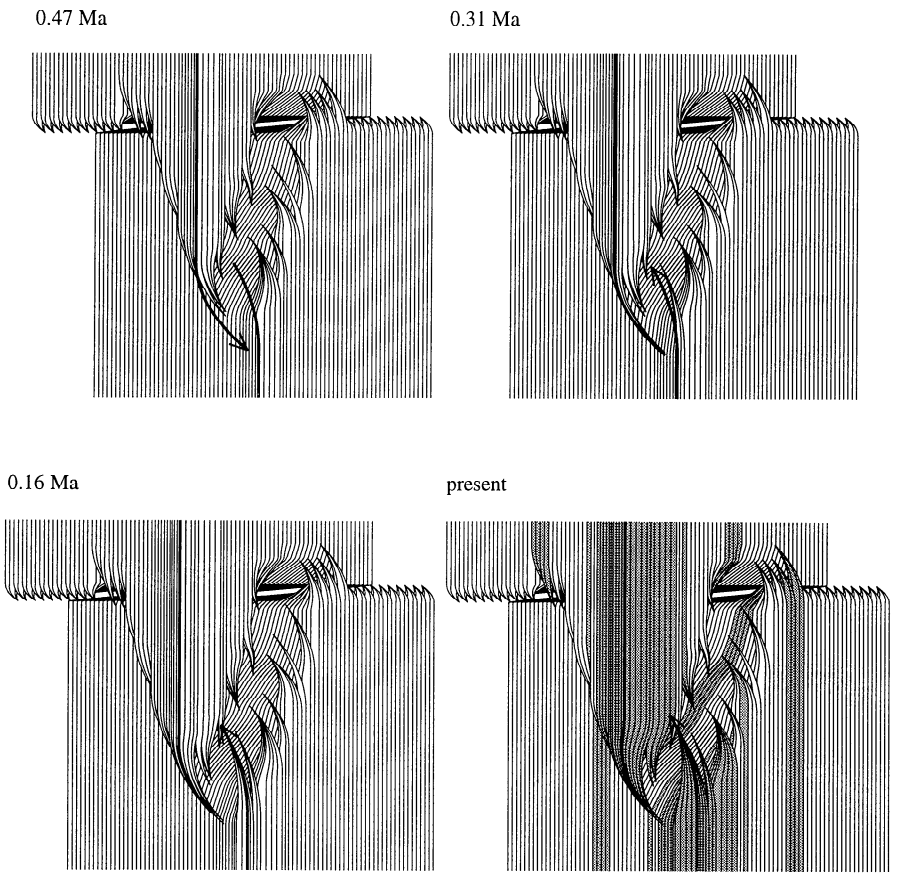

Figure 8c. The polarity of propagation changed again ~0.3 Ma, and the eastern ridge has been propagating northward to the present. Normal polarity chrons such as Brunhes, Jaramillo, and anomaly 2 are shaded in the present stage for comparison with observed magnetic lineations.

proposed outer pseudofault had enigmatic low reflectivity. In this work, the short trough is recognized as an abandoned rift (AR i) based on the ambient seafloor fabric. The tip angle reduces to ~17°, and the west flank spreads faster than the east one (Figure 7). The low seafloor reflectivity is then located outside of the pseudofault, and it belongs to older seafloor created at the western ridge. The reason for the asymmetry faster inside than outside of the overlapped ridges in spreading remains unclear.

The magnetic isochrons identified here are basically in good agreement with those identified by *Naar and Hey* [1991]. The denser magnetic profiles and the additional strike information provided by the STCM, however, delineate more detailed configuration of the isochrons with higher certainty. Especially, the Brunhes, Jaramillo, and anomaly 2 chrons of the eastern ridge show more complicated shapes (compare Figure 7 with Figure 9a of *Naar and Hey* [1991]).

Speed Limit Hypothesis

Naar and Hey [1989*b*] proposed a speed limit hypothesis that a transform fault cannot exist with a slip rate higher than 145 km/m.y. This critical slipping rate is now reduced to 136 km/m.y., based on the astronomically calibrated timescale [*Shackleton et al.*, 1990; *Hilgen*, 1991*a*, 1991*b*]. This hypothesis was based on the observation along the currently active mid-ocean ridge system; the EPR 15°S-35°S is spreading at a higher rate than the critical value, and there is no transform fault observed. That portion of the EPR comprises a smaller-scale dueling propagator at 20°40′S [*Macdonald et al.*, 1988*a*; *Perram et al.*, 1993], the Easter microplate, the dueling propagator system studied here, and the Juan Fernandez microplate. The magnetic study of the dueling propagator system with the mapping of the fracture zone reveals that the area between these two microplates has been spreading at a nearly constant rate as high as ~150 km/m.y., and a transform fault did exist at least for 1 m.y. before 2 Ma, in contradiction with the speed limit hypothesis. The hypothesis also is suggested to be null by *Bird and Naar* [1994] and *Hey et al.* [1995]. However, it is still significant that this EPR portion behaves so differently from other fast spreading centers with spreading rates less than 136 km/m.y. The studied portion of the EPR is the only part which is spreading faster than 136 km/m.y. on Earth, so it is difficult to establish reliable systematics until some past examples of comparable spreading rates are reported. The reason for the highly complex tectonics exhibited in the studied area is discussed later with causes for the dueling propagation.

Distributed Shearing or Rigid Plate Rotation?

The overlapped zone has been undergoing distributed shearing, not rotating as a rigid plate. This fact is supported by the distributed seismicity in the overlapped zone

[*Wetzel et al.*, 1993] and the abrupt changes of the side scan lineaments [*Klaus et al.*, 1991]. Therefore this nontransform offset is presently an oceanic rift propagation system with the largest offset (~120 km), which roughly doubles the propagator system at the Orozco transform fault [*Madsen et al.*, 1986, 1992]. Rigid plate rotation with an offset width of ~50 km has been proposed for the Wilkes transform system [*Goff et al.*, 1993]. The spreading rate at the Wilkes transform is 139 km/m.y. [*DeMets et al.*, 1994] so that the age offset is ~0.7 m.y. The dueling propagator studied here has a larger age offset of ~1.6 m.y., which implies that the transition from distributed shear deformation to rigid plate rotation cannot be explained only by the age offset of a propagator system.

The clockwise change in the trend of the SOEST fracture zone is as much as 9°, and the western and eastern trends of the SOEST fracture zone deviate from the trend based on NUVEL-1 by -6° and +3°, respectively (positive for counterclockwise). A recent study by *Cormier et al.* [1996] suggests that there has been a clockwise change of only a few degrees in the Pacific-Nazca spreading direction since 3 Ma. The +3° difference between the eastern trend and the predicted trend probably reflects this plate motion change. The -6° deviation of the western trend may have resulted from the rigid plate rotation in the overlapped zone from 1.95 to 1.39 Ma (Figure 8a) because a bookshelf faulting mechanism could not have produced this rotation. This possible rigid plate rotation, with a similar age offset to the current offset, indicates that another important factor for the transition from distributed shearing to rigid plate rotation may be the migration speed of an overlapped zone (M.-H. Cormier, personal communication, 1995). Because of the changes in propagation polarity, the western part of the SOEST fracture zone was trapped in the overlapped zone for ~0.56 m.y. Although this idea is highly speculative, a "stress annealing" effect for bookshelf faulting may be important for the genesis of microplates. The recent polarity change at ~0.3 Ma may be creating a similar situation, and the precursor of rigid plate rotation suggested by *Hey et al.* [1995] is consistent with the above speculation.

Causes for Dueling Propagation

Rift propagation seems to occur to seek a new stable state when some excessive forces cause instabilities on a spreading system. So far, mainly two concrete mechanisms have been proposed for rift propagation; a ridge propagates away from areas of anomalously shallow seafloor which may reflect excessive magma activity such as hotspots [*Hey et al.*, 1980; *Phipps Morgan and Parmentier*, 1985], or it propagates in response to changes in plate motion [*Hey and Wilson*, 1982; *Wilson et al.*, 1984]. The former, the hotspot-driven model, excellently fits the rift propagation on the Galapagos spreading center; all four propagators there moved or have been moving away from the hotspot located near the spreading center [*Hey et al.*, 1980; *Wilson and Hey*, 1995]. On the other hand, the general trend of the rift propagation on the Juan de Fuca ridge is consistent with the latter model [*Wilson et al.*, 1984; *Wilson*, 1988] though the correlation with hotspot activities also has been suggested for the Cobb offset [*Johnson et al.*, 1983; *Karsten and Delaney*, 1989].

The Easter hotspot, alleged to be located near Easter Island, seems to be responsible for the western ridge's propagation, as well as the propagation on the east rift of the Easter microplate [*Schilling et al.*, 1985; *Naar and Hey*, 1991]. The western ridge and the Easter east rift symmetrically propagate away from the hotspot, which somewhat resembles the situation seen at the Galapagos area. Although the Easter southwest rift propagates toward the hotspot region, it has probably resulted from the edge-driven kinematics of the microplate rotation [*Schouten et al.*, 1993] and thus may not contradict the hotspot-driven model. The axial depths along the segment E1 increase northward, which is probably related to the northward propagation. The segments E2 and E3, however, keep roughly constant axial depth; thus the ridge axis topography is not consistent with simple hotspot driven propagation. The clockwise change in the trend of the SOEST fracture zone across the ARs a–c suggests that the normal RTI was broken by the change in the Pacific-Nazca spreading direction at ~2 Ma. The northward propagation of the eastern ridge at ~1.95 Ma is consistent with the expected deviatoric stress around the RTI [*Fujita and Sleep*, 1978; *Gallo and Fox*, 1982]. Because the eastern anomaly 2 chron of the eastern ridge can be identified across the fracture zone, the intratransform origin of the rift propagation [*Bird and Naar*, 1994] does not apply to this propagator system. The transform fault existing before ~2 Ma was less than half as long as those for the Easter and Juan Fernandez microplates, and the intratransform instability may have been negligible. *Epp* [1984] proposed a change in the Pacific plate motion around 0.5 to 1 Ma based on hotspot trace analysis, which might be related to the more recent propagation events of the eastern ridge (1.21-0.99 Ma and 0.31 Ma to present). However, other hotspot trace analyses suggest earlier timings such as ~5 Ma [*Cox and Engebretson*, 1985; *Pollitz*, 1986]. Even if there were such corresponding changes in plate motion, however, it is difficult to explain the observed changes in the polarity of propagation only by changes in plate motion: a clockwise change for a left-stepping transform fault generates an excess deviatoric stress field which may initiate the northward propagation of the eastern ridge but also enhance the ongoing southward propagation of the western ridge [*Fujita and Sleep*, 1978].

It is noted that the timing of tectonic evolution appears to be very similar at the Easter and Juan Fernandez microplates and this dueling propagator, and thus the tectonics of the southern part of the Pacific-Nazca spreading center should be considered as a single objective to decipher. This portion of the EPR has anomalously shallow seafloor compared to the rest of the EPR, even if its superfast spreading rate is considered. The broad low-velocity zone (LVZ) under this region that was detected by seismic studies [e.g., *Woodhouse and Dziewonski*, 1984; *Montagner and Tanimoto*, 1991] probably causes the swell of the seafloor. Considering that the principal resisting force for rift propagation is viscous suction at the tip [*Phipps Morgan and Parmentier*, 1985; *Schubert and Hey*, 1986; *Parmentier and Schubert*, 1989], the broad LVZ weakens the effect of age offset and facilitates rift propagation. Once rift propagation has begun, therefore, it can be long-lived to develop a large offset within which the overlapped zone cannot be deformed with distributed

shear. Thus a microplate can be relatively easily created in this area. The microplate rotation probably generates complicated interplate and intraplate stresses, which may trigger off another rift propagation. In addition, it has been suggested that the length of ridge segments is important for the polarity of propagation [*Macdonald et al.*, 1991] so that the fine-scale history of the segmentation in this area should be considered to resolve the evolution of the dueling propagation. The very unique and complex spreading style along the EPR from the Easter microplate to the Juan Fernandez microplate may originate in the broad LVZ with the evolution of the distributed stresses along the spreading center.

Summary

The major tectonic components such as the western and eastern ridges, a fracture zone, and abandoned ridges were clearly recognized in the side scan data, the bathymetry, and the magnetization structure of the seafloor. These two ridges, curving toward each other, make a large overlapping spreading zone, the width and length of which are both ~120 km. The western ridge shows shallower flanks, more intense segmentation, and weaker magnetization contrasts than the eastern one. Each abandoned ridge or rift shows its own curvature, axial depth variation, and magnetization contrast, implying significant deviation from a simple cyclic rift failure. A fracture zone was mapped to the south of Easter Island, on the east flank of the western ridge. Its counterpart on the west flank could be located south of the Orongo fracture zone under the seamount chain.

The magnetic boundary strike map, combined with the downward component profiles of the vector anomalies, enabled the identification of the fine-scale magnetic lineations in spite of the sparse track density. In addition, the vector anomalies permitted the assessment of the three-dimensionality of the observed magnetic fields by the 3-D index. This quantity was used for testing the two-dimensional assumption in the magnetic inversion and also supported the reliable identification of the magnetic lineations.

The recent spreading rates at both ridges were roughly estimated by focusing on the steady state spreading portion. The western ridge has been spreading at ~135 km/m.y., and the eastern ridge has been spreading at ~150 km/m.y. The latter is consistent with the prediction of the global plate motion model (NUVEL-1A), and the slower spreading rate at the western ridge may be attributed to the existence of the Easter southwest rift located farther west of the ridge. The current propagation rate of the eastern ridge was estimated as ~500 km/m.y. based on the angle between the pseudofaults. The net propagation rate of the western ridge for the last 1.9 m.y. was also estimated to be ~120 km/m.y.

The configuration of the magnetic isochrons from Brunhes to anomaly 2A and the variation of the magnetization contrasts, as well as the geometry of the ridge axes, the abandoned ridges/rifts, and the fracture zone, provide sufficient clues for constructing the kinematics of this EPR portion during the last 2 m.y. The current dueling propagator initiated at a normal RTI around 1.9 Ma and has alternately propagated southward and northward. The eastern ridge has been propagating to the north for the last 0.3 m.y., while the dominant propagation has been the southern propagation of the western ridge. The propagation of the western ridge may have been initiated and driven by the Easter hotspot, whereas the eastern ridge lacks a clear reason for its northward propagation. As well as the fine-scale history of ridge axis segmentation, a more extensive framework including the tectonics of the Easter and the Juan Fernandez microplates is required to understand the perplexing evolution of this dueling propagator system and general processes involved with dueling propagator systems.

Acknowledgments. We gratefully acknowledge the assistance of the captain and the crew of the R/V *Melville*, the GLORI-B group led by Mike Somers, the SIO shipboard technician group led by Ron Moe, and cruise participants Fernando Martinez, Ruth Rusby, Paul Johnson, Dave Canine, Noel Ludwig, Audré Harlowe, and Tricia Allen. Nobuhiro Isezaki generously provided his STCM for the cruise. Kensaku Tamaki and Hiromi Fujimoto supported J.K.'s participation in the cruise through contract 04044044 (InterRidge Japan Project) of the Ministry of Education, Science and Culture, Japan. This participation was also supported in part by NSF grants, OCE-9116012 and OCE-9302802 to David Naar. Paul Johnson processed GLORI-B and Sea Beam 2000 side scan/bathymetry data and produced Figure 3 and Plate 1. Doug Wilson provided the "overlap" program for the kinematic modeling. Leg 5 of the GLORIA Expedition was funded by NSF grant OCE-9101341. An Associate Editor, Robert Bird, and Milene Cormier are thanked for their very careful reviews and constructive comments. Kensaku Tamaki assisted this publication with funding. WHOI contribution 9114, SOEST contribution 3963, HIGP contribution 849.

References

Anderson-Fontana, S., J. P. Engeln, P. Lundgren, R. L. Larson, and S. Stein, Tectonics and evolution of the Juan Fernandez microplate at the Pacific-Nazca-Antarctic triple junction, *J. Geophys. Res.*, *91*, 2005–2018, 1986.

Baksi, A. K., V. Hsu, M. O. McWilliams, and E. Farrar, $^{40}Ar/^{39}Ar$ dating of the Brunhes-Matuyama geomagnetic field reversal, *Science*, *256*, 356–357, 1992.

Bird, R. T., and D. F. Naar, Intratransform origins of mid-ocean ridge microplates, *Geology*, *22*, 987–990, 1994.

Carbotte, S., and K. Macdonald, East Pacific Rise 8°-10°30′N: Evolution of ridge segments and discontinuities from SeaMARC II and three-dimensional magnetic studies, *J. Geophys. Res.*, *97*, 6959–6982, 1992.

Christie, D. M., and J. M. Sinton, Evolution of abyssal lavas along propagating segments of the Galapagos spreading center, *Earth Planet. Sci. Lett.*, *56*, 321–335, 1981.

Cormier, M., D. S. Scheirer, and K. C. Macdonald, Evolution of the East Pacific Rise at 16°-19°S since 5 Ma: Splitting and rapid migration of axial discontinuities, *Mar. Geophys. Res.*, in press, 1996.

Cox, A., and D. Engebretson, Change in motion of Pacific plate at 5 Myr BP, *Nature*, *313*, 472–474, 1985.

DeMets, C., R. G. Gordon, D. F. Argus, and S. Stein, Current plate motions, *Geophys. J. Int.*, *101*, 425–478, 1990.

DeMets, C., R. G. Gordon, D. F. Argus, and S. Stein, Effect of recent revisions to the geomagnetic reversal time scale on estimates of current plate motions, *Geophys. Res. Lett.*, *21*, 2191–2194, 1994.

Engeln, J. F., and S. Stein, Tectonics of the Easter plate, *Earth Planet. Sci. Lett.*, *68*, 259–270, 1984.

Epp, D., Possible perturbation to hotspot traces and implications for the origin and structure of the Line Islands, *J. Geophys. Res.*, *89*, 11273–11286, 1984.

Francheteau, J., A. Yelles-Chaouche, and J. Craig, The Juan Fernan-

dez microplate north of the Pacific-Nazca-Antarctic plate junction at 35°S, *Earth Planet. Sci. Lett.*, *86*, 253–268, 1987.

Francheteau, J., et al., Pito and orongo fracture zones: the northern and southern boundaries of the Easter microplate (southeast Pacific), *Earth Planet. Sci. Lett.*, *89*, 363–374, 1988.

Fujita, K., and N. H. Sleep, Membrane stresses near mid-ocean ridge-transform intersections, *Tectonophysics*, *50*, 207–221, 1978.

Gallo, D. G., and P. J. Fox, Changes in relative plate motion: Propagating ridges and the generation of oceanic micro-plates along accreting plate boundaries, *Eos Trans. AGU*, *63*, 446, 1982.

Goff, J. A., D. J. Fornari, J. R. Cochran, C. Keeley, and A. Malinverno, Wilkes tranform system and "nanoplate", *Geology*, *21*, 623–626, 1993.

Hagen, R. A., N. A. Baker, D. F. Naar, and R. N. Hey, A SeaMARC II survey of recent submarine volcanism near Easter Island, *Mar. Geophys. Res.*, *12*, 297–315, 1990.

Handschumacher, D. W., J. R. H. Pilger, J. A. Foreman, and J. F. Campbell, Structure and evolution of the Easter plate, *Mem. Geol. Soc. Am.*, *154*, 63–76, 1981.

Herron, E. M., Sea-floor spreading and the Cenozoic history of the east-central Pacific, *Geol. Soc. Am. Bull.*, *83*, 1671–1692, 1972.

Hey, R. N., and D. S. Wilson, Propagating rift explanation for the tectonic evolution of the northeast Pacific–The pseudomovie, *Earth Planet. Sci. Lett.*, *58*, 167–188, 1982.

Hey, R. N., F. K. Duennebier, and W. J. Morgan, Propagating rifts on midocean ridges, *J. Geophys. Res.*, *85*, 3647–3658, 1980.

Hey, R. N., D. F. Naar, M. C. Kleinrock, W. J. Phipps Morgan, E. Morales, and J. G. Schilling, Microplate tectonics along a superfast seafloor spreading system near Easter Island, *Nature*, *317*, 320–324, 1985.

Hey, R. N., M. C. Kleinrock, S. P. Miller, T. M. Atwater, and R. C. Searle, Sea Beam/Deep-Tow investigation of an active oceanic propagating rift system, Galapagos 95.5°W, *J. Geophys. Res.*, *91*, 3369–3393, 1986.

Hey, R. N., P. D. Johnson, F. Martinez, J. Korenaga, M. L. Somers, Q. J. Huggett, T. P. LeBas, R. I. Rusby, and D. F. Naar, Plate boundary reorganization at a large-offset rapidly propagating rift, *Nature*, *378*, 167–170, 1995.

Hilgen, F. J., Astronomical calibration of Gauss to Matuyama sapropels in the Mediterranean and implication for the geomagnetic polarity time scale, *Earth Planet. Sci. Lett.*, *104*, 226–244, 1991*a*.

Hilgen, F. J., Extension of the astronomical calibrated (polarity) time scale to the Miocene/Pliocene boundary, *Earth Planet. Sci. Lett.*, *107*, 349–368, 1991*b*.

International Association of Geomagnetism and Aeronomy Division V, International geomagnetic reference field, 1991 revision, *J. Geomagn. Geoelectr.*, *43*, 1007–1012, 1991.

Isezaki, N., A new shipboard three-component magnetometer, *Geophysics*, *51*, 1992–1998, 1986.

Johnson, H. P., J. L. Karsten, J. R. Delaney, E. E. Davis, R. G. Currie, and R. L. Chase, A detailed study of the Cobb offset of the Juan de Fuca Ridge: Evolution of a propagating rift, *J. Geophys. Res.*, *88*, 2297–2315, 1983.

Johnson, P. D., Recent structual evolution of the EPR 29°S large-scale duelling propagator system, Master's thesis, Univ. of Hawaii, Honolulu, 1996.

Karsten, J. L., and J. Delaney, Hot spot-ridge crest convergence in the northeast Pacific, *J. Geophys. Res.*, *94*, 700–712, 1989.

Klaus, A., W. Icay, D. F. Naar, and R. N. Hey, SeaMARC II survey of a propagating limb of a large nontransform offset near 29°S along the fastest spreading East Pacific Rise segment, *J. Geophys. Res.*, *96*, 9985–9998, 1991.

Korenaga, J., Comprehensive analysis of marine magnetic vector anomalies, *J. Geophys. Res.*, *100*, 365–378, 1995.

Larson, R. L., R. C. Searle, M. C. Kleinrock, H. Schouten, R. T. Bird, D. F. Naar, R. I. Rusby, E. E. Hooft, and H. Lasthiotakis, Roller-bearing tectonic evolution of the Juan Fernandez microplate, *Nature*, *356*, 571–576, 1992.

Lonsdale, P., Geomorphology and structural segmentation of the crest of the southern (Pacific-Antarctic) East Pacific Rise, *J. Geophys. Res.*, *99*, 4683–4702, 1994.

Macdonald, K. C., J. C. Sempéré, and P. J. Fox, East Pacific Rise from Siqueiros to Orozco fracture zones: Along-strike continuity of axial neovolcanic zone and structure and evolution of overlapping spreading centers, *J. Geophys. Res.*, *89*, 6049–6069, 1984.

Macdonald, K. C., R. M. Haymon, S. P. Miller, J. C. Sempéré, and P. J. Fox, Deep-Tow and Sea Beam studies of dueling propagating ridges on the East Pacific Rise near 20°40′S, *J. Geophys. Res.*, *93*, 2875–2898, 1988*a*.

Macdonald, K. C., P. J. Fox, L. J. Perram, M. F. Eisen, R. M. Haymon, S. P. Miller, S. M. Carbotte, M. H. Cormier, and A. N. Shor, A new view of the mid-ocean ridge from the behavior of ridge-axis discontinuities, *Nature*, *335*, 217–225, 1988*b*.

Macdonald, K. C., D. S. Scheirer, and S. M. Carbotte, Mid-ocean ridges: Discontinuities, segments and giant cracks, *Science*, *253*, 986–994, 1991.

Madsen, J. A., P. J. Fox, and K. C. Macdonald, Morphotectonic fabric of the Orozco transform fault: Results from a Sea Beam investigation, *J. Geophys. Res.*, *91*, 3439–3454, 1986.

Madsen, J. A., D. J. Fornari, M. H. Edwards, D. G. Gallo, and M. R. Perfit, Kinematics framework of the Cocos-Pacific plate boundary from 13°N to the Orozco transform fault: Results from an extensive magnetic and SeaMARC II survey, *J. Geophys. Res.*, *97*, 7011–7024, 1992.

McKenzie, D., The geometry of propagating rifts, *Earth Planet. Sci. Lett.*, *77*, 176–186, 1986.

Montagner, J. P., and T. Tanimoto, Global upper mantle tomography of seismic velocities and anisotropies, *J. Geophys. Res.*, *96*, 20337–20351, 1991.

Naar, D. F., and R. N. Hey, Recent Pacific-Easter-Nazca plate motions, in *Evolution of Mid-Ocean Ridges*, edited by J. M. Sinton, vol. 57, Geophys. Monogr. Ser., pp. 9–30. AGU, Washington, D.C., 1989*a*.

Naar, D. F., and R. N. Hey, Speed limit for oceanic transform faults, *Geology*, *17*, 420–422, 1989*b*.

Naar, D. F., and R. N. Hey, Tectonic evolution of the Easter microplate, *J. Geophys. Res.*, *96*, 7961–7993, 1991.

Parmentier, E. M., and G. Schubert, Rift propagation, *Geophys. Res. Lett.*, *16*, 183–186, 1989.

Perram, L. J., M. H. Cormier, and K. C. Macdonald, Magnetic and tectonic studies of the dueling propagating spreading centers at 20°40′S on the East Pacific Rise: Evidence for crustal rotations, *J. Geophys. Res.*, *98*, 13835–13850, 1993.

Phipps Morgan, J., and E. M. Parmentier, Causes and rate-limiting mechanisms of ridge propagation: A fracture mechanics model, *J. Geophys. Res.*, *90*, 8603–8612, 1985.

Pollard, D. D., and A. Aydin, Propagation and linkage of oceanic ridge segments, *J. Geophys. Res.*, *89*, 10017–10028, 1984.

Pollitz, F. F., Pliocene change in Pacific-plate motion, *Nature*, *320*, 738–741, 1986.

Rusby, R. I., and R. C. Searle, A history of the Easter microplate, 5.25 Ma to present, *J. Geophys. Res.*, *100*, 12617–12640, 1995.

Schilling, J. G., H. Sigurdsson, A. N. Davis, and R. N. Hey, Easter microplate evolution, *Nature*, *317*, 325–331, 1985.

Schouten, H., K. D. Klitgold, and D. G. Gallo, Edge-driven microplate kinematics, *J. Geophys. Res.*, *98*, 6689–6701, 1993.

Schubert, G., and R. N. Hey, Mantle viscosity beneath the Galapagos 95.5°W propagating rift, *Geophys. Res. Lett.*, *13*, 329–332, 1986.

Searle, R. C., R. I. Rusby, J. Engeln, R. N. Hey, J. Zukin, P. M. Hunter, T. P. LeBas, J. J. Hoffman, and R. Livermore, Comprehensive sonar imaging of the Easter microplate, *Nature*, *341*, 701–705, 1989.

Sempere, J. C., and K. C. Macdonald, Overlapping spreading centers: Implications from crack growth simulation by the displacement discontinuity method, *Tectonics*, *5*, 151–163, 1986.

Shackleton, N. J., A. Berger, and W. R. Peltir, An alternative astronomical calibration of the lower Pleistocene timescale based on ODP Site 677, *Trans. R. Soc. Edinburgh Earth Sci.*, *81*, 251–261, 1990.

Sinton, J. M., D. S. Wilson, D. M. Christie, R. N. Hey, and J. R. Delaney, Petrologic consequences of rift propagation on oceanic spreading ridges, *Earth Planet. Sci. Lett.*, *62*, 193–207, 1983.

Somers, M. L., and Q. J. Huggett, From GLORIA to GLORI-B, *Sea Technol.*, *34*, 64–68, 1993.

Wessel, P., and W. H. F. Smith, Free software helps map and display data, *Eos Trans. AGU*, *72*, 441, 1991.

Wetzel, L. R., D. A. Wiens, and M. C. Kleinrock, Evidence from earthquakes for bookself faulting at large non-transform ridge offsets, *Nature*, *362*, 235–237, 1993.

Wilson, D. S., Tectonic history of the Juan de Fuca ridge over the last 40 million years, *J. Geophys. Res.*, *93*, 11863–11876, 1988.

Wilson, D. S., Kinematics of overlapping rift propagation with cyclic rift failure, *Earth Planet. Sci. Lett.*, *96*, 384–392, 1990.

Wilson, D. S., and R. N. Hey, History of rift propagation and magnetization intensity for the Cocos-Nazca spreading center, *J. Geophys. Res.*, *100*, 10041–10056, 1995.

Wilson, D. S., R. N. Hey, and C. Nishimura, Propagation as a mechanism of reorientation of the Juan de Fuca ridge, *J. Geophys. Res.*, *89*, 9215–9225, 1984.

Woodhouse, J. H., and A. M. Dziewonski, Mapping the upper mantle: Three-dimensional modeling of Earth structure by inversion of seismic waveforms, *J. Geophys. Res.*, *89*, 5953–5986, 1984.

Yelles-Chaouche, A., J. Franchetcau, and P. Patriat, Evolution of the Juan Fernandez microplate during the last three million years, *Earth Planet. Sci. Lett.*, *86*, 269–286, 1987.

Zukin, J. H., and J. Francheteau, A tectonic test of instantaneous kinematics of the easter microplate, *Oceanol. Acta.*, *vol. Spec. 10*, 183–198, 1990.

R. N. Hey, Hawaii Institute of Geophysics and Planetology, SOEST, University of Hawaii at Manoa, 2525 Correa Road, Honolulu, HI 96822. (email: hey@iniki.soest.hawaii.edu)

Jun Korenaga, Department of Geology and Geophysics, Woods Hole Oceanographic Institution, Woods Hole, MA 02543-1542. (email: korenaga@mit.edu)

(Received August 11, 1995; revised November 15, 1995; accepted January 9, 1996.)